Journal of Materials Chemistry

Cite this: J. Mater. Chem., 2012, 22, 12039

www.rsc.org/materials

PAPER

Chemistry and electrochemistry of concentric ring cathode $Li_{1.42}Ni_{0.25}Mn_{0.75}O_{2+\gamma}$ for lithium batteries

Dapeng Wang,[ac] Ilias Belharouak,*[a] Sabine Gallagher,[b] Guangwen Zhou[c] and Khalil Amine[a]

Received 29th February 2012, Accepted 26th March 2012
DOI: 10.1039/c2jm31285a

A co-precipitation method in a continuous stirred tank reactor was developed to synthesize the carbonate precursor $Ni_{0.25}Mn_{0.75}CO_3$ for the cathode material $Li_{1.42}Ni_{0.25}Mn_{0.75}O_{2+\gamma}$. Both the precursor and the cathode materials were studied by a variety of characterization methods in order to establish a link between the compositions, structures, and physical properties of these compounds and the electrochemical properties of the $Li_{1.42}Ni_{0.25}Mn_{0.75}O_{2+\gamma}$ cathode. The precursor particles were found to have concentric ring architectures during the co-precipitation reaction, resulting in spherical particles composed of 20 μm bulky cores around which several shells/layers formed. The variation in the number of layers grown on each precursor particle led to a wide size distribution for both the precursor and cathode compounds. Cathode particles whose sizes were above 20 μm yielded lower specific capacities due to the diminished lithium ion diffusion across the voids that separate the subsequent shells. The ring architecture of the particles can be destroyed by soft ball milling, which improves the overall electrochemical performance of the cathode.

Introduction

Today's cathode materials for lithium batteries consist of lithium transition metal oxides or phosphates. To meet today's requirements for diverse battery applications, elemental doping,[1–3] surface coating,[4–7] and/or crystal downsizing[8–10] have been pursued by researchers, with a primary focus on safety improvement and cost reduction of the materials. Earlier studies on $LiMnPO_4$,[11] $LiFePO_4$,[12] $LiNi_{1-x}Co_xO_2$,[13] $LiMn_2O_4$,[14] and $Li[Ni_{0.5}Mn_{0.5}]O_2$[15] aimed at establishing the relationship between their electrochemical properties and the size effect of the primary and secondary particles of which they were composed. However, in-depth analyses have not been performed on the inner core of the micron-size particles, the consequence of which was lack of understanding of lithium insertion and diffusion with respect to quantifiable properties such as the specific capacity and rate capability of these materials. The present study provides comprehensive structural, chemical, physical, thermal, morphological, and surface analyses on cathode particles grown in a continuous stirred tank reactor (CSTR). Co-precipitation of battery carbonate precursors using CSTRs has several advantages, as discussed in our previous work;[16–20] however, the inhomogeneity in the growth of the particles has led to materials with unsatisfactory electrochemical performance, particularly for the particles above 20 μm. This observation sparked our desire to investigate the interior structure of these large particles and to determine the relationship between their electrochemical properties and internal morphologies.

Experimental

Nickel sulfate hexahydrate ($NiSO_4 \cdot 6H_2O$), manganese sulfate monohydrate ($MnSO_4 \cdot H_2O$), sodium carbonate (Na_2CO_3), and ammonium hydroxide ($NH_3 \cdot H_2O$) were used as the starting materials to prepare the $Ni_{0.25}Mn_{0.75}CO_3$ precursor. For a schematic of the setup for the water-jacketed CSTR system and detailed experiment parameters, refer to our former report.[17] The precursor material was collected from hour 5 to hour 12 of the CSTR process. Collected samples were washed with hot water several times to remove residual sodium and sulfuric species, then filtered and dried inside a vacuum oven set at 100 °C over 24 hours. Finally, about 2 kg dark brown precursor was harvested.

We prepared $Li_{1.42}Ni_{0.25}Mn_{0.75}O_{2+\gamma}$ cathode materials using appropriate amounts of $Ni_{0.25}Mn_{0.75}CO_3$ and Li_2CO_3. The mixture was calcined at 900 °C for 15 hours. The synthesized cathode materials were sieved with different size screens and classified into three groups according to their sizes: less than 20 μm, 20–38 μm, and 38–75 μm. The electrochemical properties of the cathode materials before and after sieving were evaluated in CR-2032 type cells. The positive electrode was made by mixing 80% active material, 10% acetylene black, and 10% polyvinylidene difluoride binder using a THINKY mixer for 3 minutes (2000 rpm) followed by a defoaming process for

[a]Argonne National Laboratory, Chemical Sciences and Engineering Division, 9700 S. Cass Ave., Argonne, IL 60439, USA. E-mail: belharouak@anl.gov
[b]Argonne National Laboratory, Energy Systems Division, 9700 S. Cass Ave., Argonne, IL 60439, USA
[c]State University of New York at Binghamton, Binghamton, NY 13902, USA

1 minute (2200 rpm). This process was repeated several times to ensure high homogeneity between the ingredients. The resulting slurry was coated onto an aluminium foil. Cells were assembled inside a helium-filled glove box with lithium metal as the counter anode. A Celgard 2325 membrane was used as the separator. The electrolyte was 1.2 M $LiPF_6$ dissolved in ethylene carbonate and ethyl methyl carbonate in a ratio of 3 : 7 (vol%). The cells were tested in the voltage range of 2.0–4.6 V at a constant current density of 20 mA g^{-1} at room temperature.

Morphologies of the precursor and cathode materials were characterized with cold field emission scanning electron microscopy (SEM, Hitachi S-4700-II). Bisections of cathode particles were prepared with an ultra-microtome. Line mapping with energy dispersive X-ray spectrometry (EDXS) was used to qualitatively determine the local Mn/Ni atomic ratio inside the cathode particles. Chemical compositions of the cathode materials were analyzed by ion coupled plasma (ICP). Particle size distributions were measured with a particle size analyzer (Cilas1090). X-ray powder diffraction (XRD) of the precursor was recorded with a D5000 Siemens X-ray diffractometer, using a Cu-Kα radiation source (λ = 1.5406 Å). The samples were scanned from 5 to 80° at a rate of 0.02° per 20 s. For the cathode materials, powder XRD studies were performed at Argonne's Advanced Photon Source, station 11-ID-C. A small amount of the sample was placed into a 0.33 mm diameter Kapton capillary (0.01 mm wall thickness), filling approximately 3–5 mm height of the capillary. After the capillary was sealed, XRD data were collected with a 2-D image plate detector. The wavelength (λ = 0.10798 Å) and sample-to-detector distance (d = 180 mm, giving a usable range of d-spacing of 1.34–40 Å) were calibrated using CeO_2 as a reference material. The collection of diffraction data proceeded for 10 s; the time of the processing of the image-plate data was 125 s, giving a total time for a single measured data set of 135 s. The decomposition of the precursor was investigated with thermal gravimetric analysis (TGA) coupled with mass spectroscopy (MS) and Fourier transform infrared spectroscopy (FTIR).

Results and discussion

Material characterization

Carbonate co-precipitation by the CSTR method was employed to prepare precursor materials that can be used to produce large quantities of cathode materials for lithium-ion batteries. Because of the continuous stirring in this method, the carbonate precursor particles formed and trapped within the reactor walls can undergo significant growth, as outlined in our previous work.[17] In our experimental setup, the precursor $Ni_{0.25}Mn_{0.75}CO_3$ was continuously collected for 7 hours after the solution reached steady state.

The XRD pattern of the collected precursor $Ni_{0.25}Mn_{0.75}CO_3$ is shown in Fig. 1. The material was a single phase and could be indexed based on the $R3c$ space group of $MnCO_3$. Despite the broadness of the diffraction peaks, which was previously attributed to the small grain size of the primary particles (17 nm according to the Scherrer equation based on the (104) diffraction peak), $(Ni_{0.25}Mn_{0.75})CO_3$ is iso-structural with $MnCO_3$, where a part of the manganese is replaced by nickel within the carbonate matrix. In this case, we refined the structure of $Ni_{0.25}Mn_{0.75}CO_3$ using the Rietveld method and adopting the structural model of $MnCO_3$ ($R3c$ space group). The refined lattice parameters of $(Ni_{0.25}Mn_{0.75})CO_3$ are $a = b$ = 4.803 Å and c = 15.602 Å, which are close to those of $MnCO_3$ ($a = b$ = 4.773 Å and c = 15.642 Å[21]).

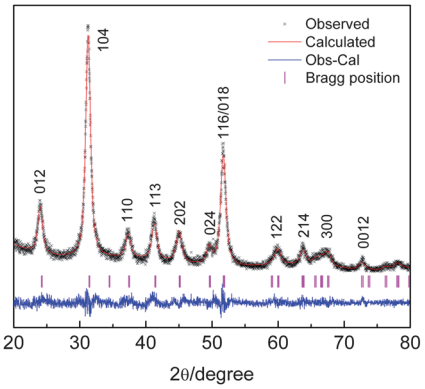

Fig. 1 X-ray diffraction pattern of the synthesized carbonate precursor. The black curve is the observed diffraction pattern, and the red curve is the calculated diffraction pattern. The Bragg position (pink lines) is based on pdf # 01-086-0172 44-1472 in the ICSD database.

The morphology and particle size distribution of $(Ni_{0.25}Mn_{0.75})CO_3$ are shown in Fig. 2. The particles, in general, seemed to be dense and spherical with smooth surfaces. They had sizes, however, ranging from 15 to 50 μm. The particle size distribution measured by laser diffraction primarily exhibited a broad and symmetric peak centered at 30 μm (inset in Fig. 2). We anticipate that the particles above 20 μm would neither be suitable for electrode fabrication nor yield high electrochemical performance. However, particle size fluctuation is expected in the synthesis of large quantities of materials. Attaining more consistent size distribution, whether by engineering controls or particle size selection, would be detrimental to promoting the electrochemical properties. The surface area of the particles determined by the BET method was 150 m^2 g^{-1}, indicating that the particles had a high porosity despite the dense appearance. This finding confirmed that the particles were porous secondary agglomerates made of nanosize primary particles. On the one

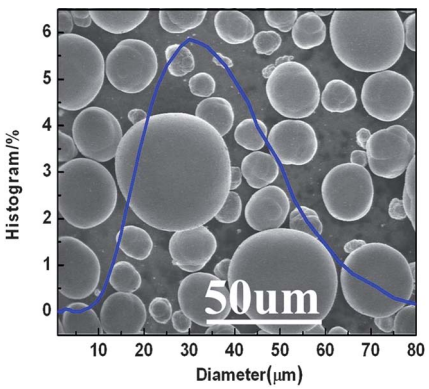

Fig. 2 Particle size distribution curve superimposed on the SEM image of the synthesized carbonate precursor.

hand, the high porosity could improve lithium diffusion if cathodes synthesized by these precursors retained their porous character. On the other hand, the high specific surface area renders the precursor particles vulnerable to moisture. For this reason, special care with regard to precursor drying and storage was taken to avoid fluctuation from batch to batch. To be specific, the as-prepared precursor particles were dried at 100 °C under vacuum for 24 hours and then were stored in a controlled-environment sealed box.

We used a TGA apparatus coupled with MS-FTIR systems to characterize the precursor materials during their thermal decomposition from room temperature to 950 °C. Fig. 3 assembles the TGA curve (Fig. 3a), TGA first-derivative curve (Fig. 3b), CO_2-evolution MS curve (Fig. 3c), and CO_2-evolution FTIR curve collected at a wavenumber of 2350 cm^{-1} (Fig. 3d) for the $Ni_{0.25}Mn_{0.75}CO_3$ precursor. The TGA first derivatives were plotted to study thermal phenomena that may not be easily detectible in the TGA curve. These experiments were conducted under a high-purity dry nitrogen atmosphere. Purchased $MnCO_3$ and $NiCO_3 \cdot xH_2O$ (only nickel carbonate form available) were also subjected to these experiments for the purpose of comparison.

The TGA curves (Fig. 3a and b) indicated that $MnCO_3$ had an abrupt overall weight loss of 35% at 465 °C, which is associated with the loss of CO_2 to yield MnO and possibly some Mn_2O_3 due to the partial oxidation of MnO. The curves for $NiCO_3 \cdot xH_2O$ had mainly two thermal events: one that occurred between room temperature and 220 °C with a maximum at 130 °C, and the other, between 220 and 450 °C with a maximum at 315 °C (Fig. 3a and b). These events were attributed primarily to the loss of water and CO_2, respectively. However, the MS and FTIR curves (Fig. 3c and d) of $NiCO_3 \cdot xH_2O$ revealed a positive CO_2 uptake starting at 100 °C. This shift signifies that along with the removal of adsorbed water, some CO_2 species were removed as well. The same observation can be made for $MnCO_3$, whose thermal decomposition started at a much lower temperature, 230 °C, and resulted in CO_2 evolution, as is evident from Fig. 3c. These results amplify the usefulness of the MS tool because we could clearly observe CO_2 gas produced at very low temperatures, which was not detected with TGA only.

The TGA curve of $Ni_{0.25}Mn_{0.75}CO_3$ has several complex thermal features starting at around 100 °C and indicates 34 wt% weight loss at 630 °C (Fig. 3a). Despite the complexity, the TGA features of $Ni_{0.25}Mn_{0.75}CO_3$ include all the TGA features observed for both $NiCO_3 \cdot xH_2O$ and $MnCO_3$ but with some temperature shifts (Fig. 3b–d). We mainly noted that $Ni_{0.25}Mn_{0.75}CO_3$ had positive MS and FTIR signals for CO_2 starting at around 100 °C, as was also observed for $NiCO_3 \cdot xH_2O$. At this low temperature, water removal could be also possible, although the material had been dried for 24 hours in a vacuum oven, and a positive MS signal for H_2O was not obtained. In our previous paper, we demonstrated that the growth of manganese and nickel carbonate precursors begins with nickel hydroxide seed particles. In general, the earlier thermal phenomena noted for $Ni_{0.25}Mn_{0.75}CO_3$ resemble those noted for $NiCO_3 \cdot xH_2O$, and the later phenomena resemble those observed for $MnCO_3$. In a perfect solid solution of $Ni_{0.25}Mn_{0.75}CO_3$, where nickel is randomly distributed within the manganese carbonate structure, the thermal behavior of $Ni_{0.25}Mn_{0.75}CO_3$ would mainly incorporate the thermal behavior of $MnCO_3$. However, the decomposition of $Ni_{0.25}Mn_{0.75}CO_3$ at low temperature was quite similar to that of $NiCO_3 \cdot xH_2O$. Therefore, even though XRD showed that $Ni_{0.25}Mn_{0.75}CO_3$ had a strong analogy with $MnCO_3$, the real structure of this compound could also contain a structural feature derivative of $NiCO_3 \cdot xH_2O$.

Next, we mixed $Ni_{0.25}Mn_{0.75}CO_3$ with Li_2CO_3 and calcined the mixture at 900 °C to prepare $Li_{1.42}Ni_{0.25}Mn_{0.75}O_{2+\gamma}$. Unlike a previous report,[22] the as-prepared material had a low specific capacity of only 155 mA h g^{-1} (discussed later), which could be due to the wide particle size distribution that the material preserved from the precursor (Fig. 4a and e). To investigate this matter, we classified the $Li_{1.42}Ni_{0.25}Mn_{0.75}O_{2+\gamma}$ secondary particles into three size groups by sieving the as-prepared material: below 20 μm, between 20 μm and 38 μm, and above 38 μm. The morphology and particle size distributions of the

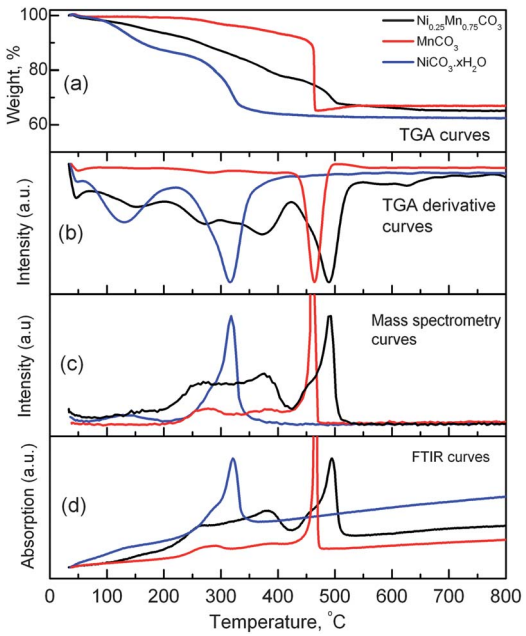

Fig. 3 TGA-MS-FTIR results for precursor materials during thermal decomposition from room temperature to 950 °C.

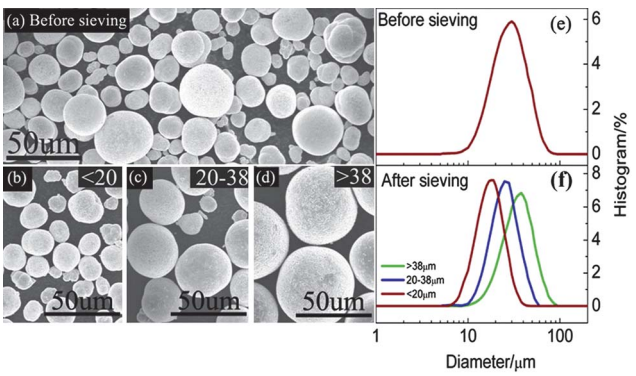

Fig. 4 Cathode morphologies and particle size distributions before and after sieving.

$Li_{1.42}Ni_{0.25}Mn_{0.75}O_{2+\gamma}$ before and after sieving are shown in Fig. 4. Before sieving, the cathode material had a wide particle size distribution, with a peak centered at 30 μm (Fig. 4e), similar to $Ni_{0.25}Mn_{0.75}CO_3$. Fig. 4f plots the three particle size distributions, which are centered at 15 μm (red solid line), 25 μm (blue solid line), and 40 μm (green solid line), respectively.

Fig. 5 compares the primary particle sizes of the samples sieved below 20 μm (Fig. 5a), between 20 μm and 38 μm (Fig. 5b), and above 38 μm (Fig. 5c). After calcination, the primary particles of all samples shared polyhedral facets and had an average particle size between 100 and 300 nm. Also, we observed porosity between the primary particles, which could be useful for facilitating the penetration of electrolyte into the inner core of the secondary particles and, therefore, improve the overall electrochemical performance of the samples. Based on these observations, the lithium diffusion rate into the primary particles is expected to be more or less the same for all sieved samples.

Thereafter, EDXS (Fig. 6) was performed on cross-sectioned particles of $Ni_{0.25}Mn_{0.75}CO_3$ and $Li_{1.42}Ni_{0.25}Mn_{0.75}O_{2+\gamma}$ along the diameters of the samples sieved below 20 μm (Fig. 6a), between 20 μm and 38 μm (Fig. 6b), and above 38 μm (Fig. 6c). This experiment was conducted primarily to check the manganese and nickel compositions across the secondary particles of both the precursor and lithiated compounds after sieving. Nickel and manganese atomic percentages are shown as green and red lines, respectively, in Fig. 6. For all samples, we observed small fluctuations around the nominal atomic percentages (25% Ni and 75% Mn). This finding indicates that the chemical composition was relatively homogeneous for the precursors and cathode materials within the composition analysis limits of EDXS. One of the interesting observations was a "core–shell" type morphology in both the precursor and cathode materials, which was manifested as concentric circular rings for larger particles (Fig. 6). The interfaces between these layers can be distinguished by darker contrasts in the case of the precursors, whereas, in the case of cathode samples, the interfaces evolved into clear voids separating the nearby layers. The number of concentric rings increased with the increase in secondary particle size. Indeed, for particles below 20 μm, only one interface could be observed separating a core of about 15 μm and a thinner shell. For the particles larger than 38 μm, up to 10 rings could be found. The solid core and subsequent rings of the $Li_{1.42}Ni_{0.25}Mn_{0.75}O_{2+\gamma}$ cathode sample are clearly visible in the high-magnification SEM image in Fig. 7. Selected area electron diffraction (SAED) results confirmed the existence of the core–shell morphology as reported in our previous work.[22] The cohesion between the adjacent dense

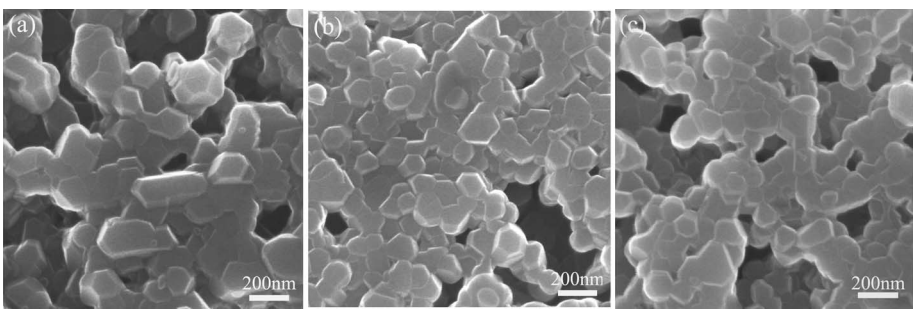

Fig. 5 SEM images of cathode materials with different secondary particle sizes: (a) less than 20 μm, (b) 20–38 μm, and (c) larger than 38 μm (images are magnifications of the surface of secondary particles).

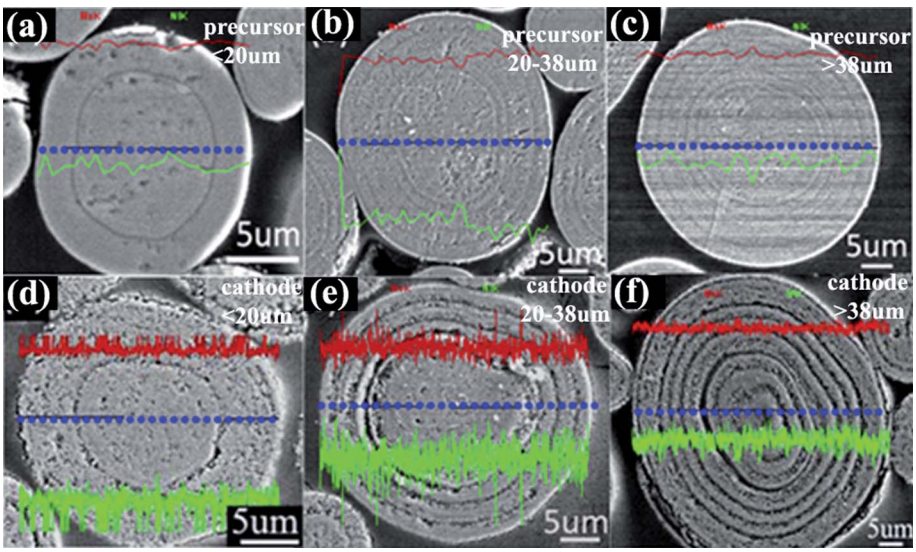

Fig. 6 EDXS curves superimposed on SEM images of bisected precursors with particle sizes of (a) <20 μm, (b) 20–38 μm, and (c) 38–75 μm and cathode materials with particle sizes of (d) <20 μm, (e) 20–38 μm, and (f) 38–75 μm.

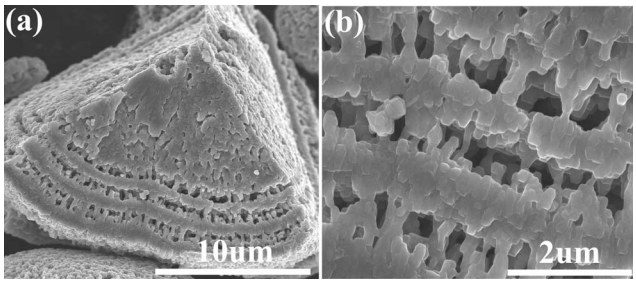

Fig. 7 SEM images of cathode materials with core–shell like features: (a) low magnification image and (b) higher magnification image of local area.

rings is ensured through the continuity between the dendritic particles grown on each side of the rings. The high porosities observed between the dense rings could be useful for electrolyte impregnation across the layers. However, because the dense character of the rings could lead to the blockage of electrolyte, lithium diffusion between the outer and inner rings and the core of the particles could be inhibited.

Because of the difference in secondary particle sizes, we suspected that, during calcination with lithium carbonate, the cathode sample particles may have different degrees of lithiation, depending upon their sizes. To investigate this hypothesis, high-energy XRD and ICP were used to characterize the structure and chemical composition of the lithiated samples after sieving. The XRD patterns of all samples are shown in Fig. 8. All of the cathodes with different particle sizes can be mainly indexed to the $R\bar{3}m$ space group, and matched well with the diffraction pattern of $LiNi_{0.5}Mn_{0.5}O_2$ reference material (bottom of Fig. 8).[23] The small additional peaks between 20 and 23° (2θ) are usually assigned to Li^+ and Mn^{4+} order in the manganese layer of the Li_2MnO_3 component in this material.[24] Essentially, we did not notice a measurable difference between the diffraction patterns for the samples sieved below 20 μm, between 20 μm and 38 μm, and above 38 μm. In fact, the calculated cell parameters obtained using Rietveld refinements (Table 1) were found to be similar for the different samples. Furthermore, the ICP results presented in Table 2 do not reveal any significant deviation in the Mn/Ni atomic ratio among the samples. However, the compositions in all samples were slightly lean in nickel, possibly due to the incomplete precipitation of nickel during the co-precipitation process. This point was discussed in our previous report.[17]

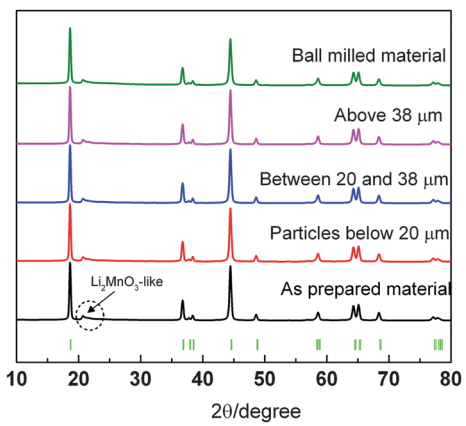

Fig. 8 High-energy XRD patterns for cathodes with different particle sizes.

Table 1 Cell parameters after Rietveld refinement

Sample	a (Å)	b (Å)	c (Å)	Cell volume (Å^3)	c/a
Pristine	2.862(8)	2.862(8)	14.267(2)	101.266(7)	4.98(3)
>38 μm	2.862(7)	2.862(7)	14.266(9)	101.259(6)	4.98(3)
20–38 μm	2.862(9)	2.862(9)	14.268(2)	101.279(7)	4.98(3)
<20 μm	2.862(7)	2.862(7)	14.268(8)	101.274(4)	4.98(4)

Table 2 ICP result of cathode materials with different particle sizes

Sample	Mn (atomic%)	Ni (atomic%)	Mn/Ni (atomic ratio)	Li/(Mn + Ni) (atomic ratio)
<20 μm	75.6 ± 5.3	24.380 ± 1.7	3.10 ± 0.22	1.49 ± 0.11
20–38 μm	75.9 ± 5.4	24.111 ± 1.7	3.14 ± 0.22	1.52 ± 0.11
>38 μm	75.9 ± 5.4	24.065 ± 1.7	3.15 ± 0.22	1.50 ± 0.11

Cell testing

The charge–discharge profiles and capacities of lithium cells made of size-selected $Li_{1.42}Ni_{0.25}Mn_{0.75}O_{2+\gamma}$ electrodes are compared to those of the as-prepared $Li_{1.42}Ni_{0.25}Mn_{0.75}O_{2+\gamma}$ in Fig. 9. The current density was 20 mA g^{-1}, which is equivalent to C/10 assuming that 200 mA g^{-1} is achieved at the 1C rate. The cell was initially charged to 4.8 V, discharged to 2 V, and then cycled between 2 and 4.6 V in the subsequent cycles. The charge capacity of the as-prepared sample containing a broad range of particle sizes (Fig. 9a) was quite similar to that of all size-selected samples (Fig. 9b–d), which was around 250 mA h g^{-1}. The first discharge capacities were 176 mA h g^{-1} (particles below 20 μm), 170 mA h g^{-1} (between 20 and 38 μm), and 162 mA h g^{-1} (above 38 μm). These results indicate that the smaller the particles, the higher the discharge capacity. The as-prepared material, which had a wide particle size distribution, delivered a discharge

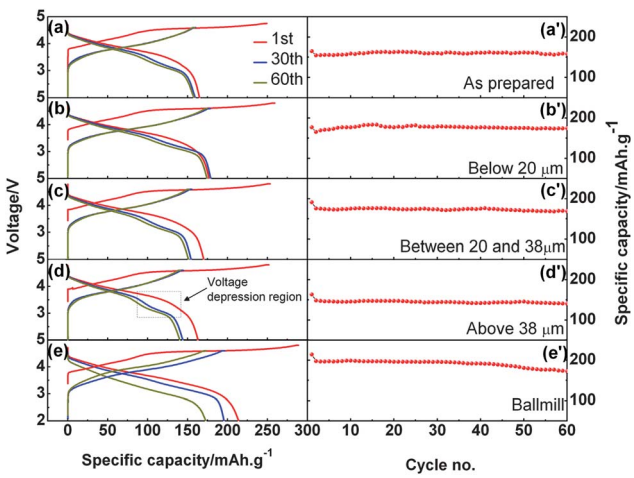

Fig. 9 Electrochemical performance of cells prepared with cathodes with different particle sizes: left, voltage–capacity profile; right, cycling performance. The current density was 20 mA g^{-1}, which is equivalent to C/10 assuming that 200 mA g^{-1} is achieved at the 1C rate.

capacity of 164 mA h g^{-1}, close to that of the material composed of the largest particles (above 38 μm).

Starting from the second cycle, the cells with electrodes composed of size-selected particles and as-prepared material (Fig. 9a′–d′) showed good capacity retention over 60 cycles. The cells made of the smaller particle electrodes showed lower capacity fade. The low capacity observed for the large particle electrode may have been due to the texture of the concentric rings within the particles. As mentioned above, effective lithium diffusion would be difficult from a massive ring to a subsequent one because of the voids that exist between these rings, which can increase the interfacial resistance within the larger particles. Therefore, the core of such particles may not be fully activated, and thus lower capacities are to be expected. We also speculate that these particles could be vulnerable to mechanical stress, which could result in pulverization during calendering.

To verify this hypothesis, we used low-energy ball milling to break down the secondary particles so that larger material surfaces would be electrochemically activated. The cathode sample was ball-milled for 1 hour in a planetary ball miller. The ball-milled sample exhibited spherical fragments, as shown in Fig. 10. After the ball milling, the particle size distribution of the sample became narrower (curve in Fig. 10) compared to the as-prepared sample (Fig. 4e), and the surface area became larger, 6 m^2 g^{-1} (ball-milled sample) *vs.* 1 m^2 g^{-1} (as-prepared sample). Subsequently, lithium cells were made of the ball-milled sample and cycled under the same conditions mentioned above (Fig. 9e). As expected, the cell exhibited a drastic increase in the initial charge and discharge capacities, 290 and 215 mA h g^{-1}, respectively, as compared with 250 and 176 mA h g^{-1} for the electrodes whose particles were below 20 μm (Fig. 9e and b). However, because of the larger surface area, which usually promotes side reactions, the capacity gradually faded upon consecutive cycling to 4.6 V. The voltage profile during the discharge of the ball-milled electrode did not show the voltage depression in the 3 V region compared to the electrodes prepared from samples before ball milling, despite the occurrence of an overall voltage drop. Furthermore, the 3 V voltage depression region seemed to be more pronounced for the electrodes with larger particle sizes

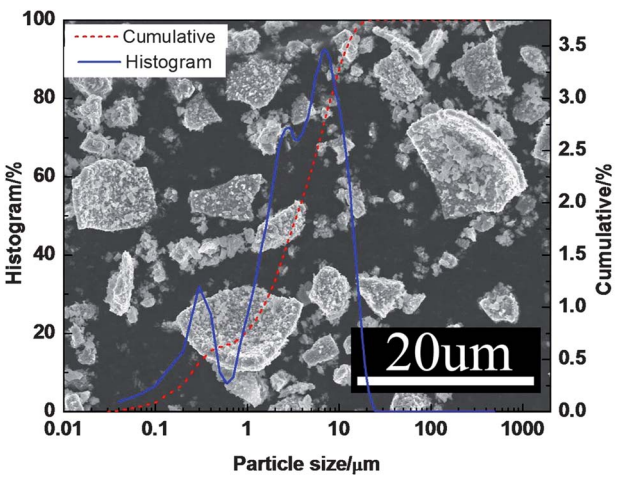

Fig. 10 Particle size distribution superimposed on the SEM image of cathode materials after ball milling.

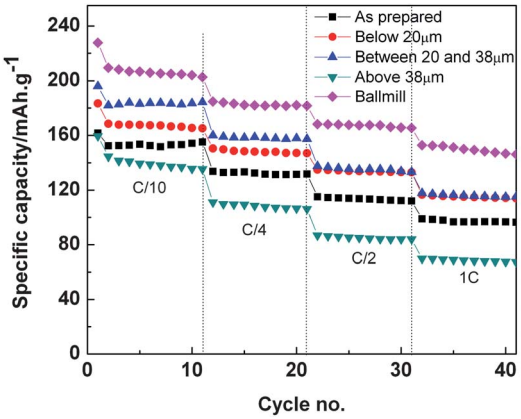

Fig. 11 Rate performance of half cells prepared with cathodes of different secondary particle sizes. Rates based on the assuming 200 mA g^{-1} is achieved at the 1*C* rate.

compared to those with smaller sizes. The reason for this difference is still under investigation, although the main factors that exacerbated the voltage depression seemed to be linked to particle size and surface area of the material.

The rate performances of all samples are shown in Fig. 11. The cells were initially cycled between 2 and 4.8 V for 1 cycle under a *C*/10 rate to activate the electrode material, and then cycled between 2 and 4.6 V at *C*/10, *C*/4, *C*/2, and 1*C* for 10 cycles per step. In general, the capacity retention of all samples declined with the rate increase (Fig. 11). However, higher capacities were achieved for the samples composed with smaller particle sizes. For example, at the 1*C* rate the specific capacities were 152 mA h g^{-1} (ball-milled sample), 115 mA h g^{-1} (samples below 20 μm and 20–38 μm), 97 mA h g^{-1} (as-prepared sample), and 67 mA h g^{-1} (sample above 38 μm). The results clearly show that the rate capability is strongly dependent upon the particle size of the samples. Also, the inner ring texture by which the large particles are constructed could have contributed to the worsening of the lithium diffusion and kinetics.

Conclusion

Systematic investigations including morphological, structural, compositional, and electrochemical characterizations were conducted on the cathode material $Li_{1.42}Ni_{0.25}Mn_{0.75}O_{2+\gamma}$ with three ranges of secondary particle size. These samples were prepared from co-precipitated carbonate precursors in a CSTR. The cathode samples were found to contain secondary particles composed of highly crystalline polyhedral primary particles, with average size around 100 nm, regardless of the secondary particle size. The particles larger than 20 μm developed concentric ring layers within their cores, which compromised the overall electrochemical performance in terms of capacity and rate capability due to the sequential void that separates the inner layers. Ball milling improved the electrochemical performance; however, it also accelerated side reactions between the electrode and electrolyte at high operating voltage, leading to gradual capacity loss with cycling. Note that we used the milling method for the purpose of proof of concept only, because it cannot ensure long-term cathode functionality due to the occurrence of side

reactions. The following approaches should be investigated for obtaining high capacity and stable materials *via* the carbonate co-precipitation method: (1) prevention of growth of the precursor particles above 20 μm during co-precipitation; (2) optimization of the Li/transition metal ratio because the particles have Ni-hydroxide enriched cores and are sensitive to moisture; and (3) determination of the proper balance between porosity and surface area of particles because the former is suited for improving the capacity and rate capability and the latter is unsuited for long life due to parasitic side reactions.

Acknowledgements

The submitted manuscript has been created by UChicago Argonne, LLC, Operator of Argonne National Laboratory ("Argonne"). Argonne, a U.S. Department of Energy Office of Science laboratory, is operated under contract no. DE-AC02-06CH11357. The U.S. Government retains for itself, and others acting on its behalf, a paid-up nonexclusive, irrevocable worldwide license in the said article to reproduce, prepare derivative works, distribute copies to the public, and perform publicly and display publicly, by or on behalf of the Government. This research was funded by the U.S. Department of Energy, Freedom CAR, and Vehicle Technologies Office. The electron microscopy was accomplished at the Electron Microscopy Center for Materials Research at Argonne National Laboratory, a U.S. Department of Energy Office of Science Laboratory operated under contract no. DE-AC02-06CH11357 by UChicago Argonne, LLC. We also thank N. L. Dietz Rago for ultramicrotome work and Chi-Kai Lin for high energy X-ray diffractions.

References

1 J. F. Ni, H. H. Zhou, J. T. Chen and X. X. Zhang, *Mater. Lett.*, 2005, **59**, 2361–2365.
2 S. Y. Chung, J. Bloking and Y. M. Chiang, *Nat. Mater.*, 2002, **1**, 123–128.
3 S. H. Kang, J. Kim, M. E. Stoll, D. Abraham, Y. K. Sun and K. Amine, *J. Power Sources*, 2002, **112**, 41–48.
4 S. T. Myung, K. Izumi, S. Komaba, Y. K. Sun, H. Yashiro and N. Kumagai, *Chem. Mater.*, 2005, **17**, 3695–3704.
5 N. V. Kosova and E. T. Devyatkina, *J. Power Sources*, 2007, **174**, 959–964.
6 S. K. Hua, G. H. Cheng, M. Y. Cheng, B. J. Hwang and R. Santhanam, *J. Power Sources*, 2009, **188**, 564–569.
7 Y. Y. Huang, J. T. Chen, J. F. Ni, H. H. Zhou and X. X. Zhang, *J. Power Sources*, 2009, **188**, 538–545.
8 J. Hassoun, G. Mulas, S. Panero and B. Scrosati, *Electrochem. Commun.*, 2007, **9**, 2075–2081.
9 F. Belliard, P. A. Connor and J. T. S. Irvine, *Solid State Ionics*, 2000, **135**, 163–167.
10 F. Belliard and J. T. S. Irvine, *J. Power Sources*, 2001, **97–98**, 219–222.
11 T. Drezen, N. H. Kwon, P. Bowen, I. Teerlinck, M. Isono and I. Exnar, *J. Power Sources*, 2007, **174**, 949–953.
12 M. Gaberscek, R. Dominko and J. Jamnik, *Electrochem. Commun.*, 2007, **9**, 2778–2783.
13 W. Li and J. C. Currie, *J. Electrochem. Soc.*, 1997, **144**, 2773–2779.
14 C. H. Lu and S. W. Lin, *J. Power Sources*, 2001, **97–98**, 458–460.
15 K.-S. Lee, S.-T. Myung, J.-S. Moon and Y.-K. Sun, *Electrochim. Acta*, 2008, **53**, 6033–6037.
16 S.-H. Park, S.-H. Kang, I. Belharouak, Y. K. Sun and K. Amine, *J. Power Sources*, 2008, **177**, 177–183.
17 D. P. Wang, I. Belharouak, G. M. Koenig, G. W. Zhou and K. Amine, *J. Mater. Chem.*, 2011, **21**, 9290–9295.
18 H. X. Deng, I. Belharouak, Y.-K. Sun and K. Amine, *J. Mater. Chem.*, 2009, **19**, 4510–4516.
19 G. M. Koenig, I. Belharouak, H. X. Deng, Y. K. Sun and K. Amine, *Chem. Mater.*, 2011, **23**, 1954–1963.
20 G. M. Koenig, I. Belharouak, H. X. Deng, H. M. Wu and K. Amine, *Electrochim. Acta*, 2011, **56**, 1426–1431.
21 ICSD database at http://icsd.fiz-karlsruhe.de/icsd/jsp/index.jsp, with pdf # 01-086-0172 44-1472 for $MnCO_3$ and pdf # 01-078-0210 12-771 for $NiCO_3$ respectively.
22 H. X. Deng, I. Belharouak, R. E. Cook, H. M. Wu, Y. K. Sun and K. Amine, *J. Electrochem. Soc.*, 2010, **157**, A447–A452.
23 Y. Y. Hinuma, Y. S. Meng, K. Kang and G. Ceder, *Chem. Mater.*, 2007, **19**, 1790–1800.
24 I. Belharouak, G. M. Koenig Jr, J. Ma, D. P. Wang and K. Amine, *Electrochem. Commun.*, 2011, **13**, 232–236.